Sequential combination therapy of ovarian cancer with degradable *N*-(2-hydroxypropyl)methacrylamide copolymer paclitaxel and gemcitabine conjugates

Rui Zhang[a], Jiyuan Yang[a], Monika Sima[a], Yan Zhou[a], and Jindřich Kopeček[a,b,1]

[a]Department of Pharmaceutics and Pharmaceutical Chemistry, Center for Controlled Chemical Delivery, and [b]Department of Bioengineering, University of Utah, Salt Lake City, UT 84112

Edited by David A. Tirrell, California Institute of Technology, Pasadena, CA, and approved July 10, 2014 (received for review April 3, 2014)

For rapid and effective clinical translation, polymer-based anticancer therapeutics need long circulating conjugates that produce a sustained concentration gradient between the vasculature and solid tumor. To this end, we designed second-generation backbone-degradable diblock *N*-(2-hydroxypropyl)methacrylamide (HPMA) copolymer carriers and evaluated sequential combination therapy of HPMA copolymer-paclitaxel and HPMA copolymer-gemcitabine conjugates against A2780 human ovarian carcinoma xenografts. First, extensive in vitro assessment of administration sequence impact on cell cycle, viability, apoptosis, migration, and invasion revealed that treatment with paclitaxel conjugate followed by gemcitabine conjugate was the most effective scheduling strategy. Second, in an in vivo comparison with first-generation (nondegradable, molecular weight below the renal threshold) conjugates and free drugs, the second-generation degradable high-molecular weight conjugates showed distinct advantages, such as favorable pharmacokinetics (three- to five-times half-life compared with the first generation), dramatically enhanced inhibition of tumor growth (complete tumor regression) by paclitaxel and gemcitabine conjugate combination, and absence of adverse effects. In addition, multimodality imaging studies of dual-labeled model conjugates confirmed the efficacy of second-generation conjugates by visualizing more than five-times enhanced tumor accumulation, rapid conjugate internalization, and effective intracellular release of payload. Taken together, the results indicate that the second-generation degradable HPMA copolymer carrier can provide an ideal platform for the delivery of a range of antitumor compounds, which makes it one of the most attractive candidates for potential clinical application.

macromolecular therapeutics | EPR effect | dual-isotope label

In the past decades, numerous polymers have been developed as drug carriers, but so far only a few progressed to clinical evaluation, such as *N*-(2-hydroxypropyl)methacrylamide (HPMA) copolymer-drug conjugates (1–3). Results from clinical trials with first-generation HPMA conjugates (4–6) indicated a significant decrease of adverse effects compared with small-molecule drugs; however, the therapeutic efficacy did not match the data in preclinical animal studies. The most likely reason is that the molecular weight (Mw) of first-generation HPMA copolymer conjugates used in the trials was only 25 kDa, not large enough to ensure sufficient circulation time in the human body and sufficient extravasation of the conjugates at the tumor by enhanced permeability and retention (EPR) effect (7). Consequently, tumors were not exposed to effective drug concentrations. For prolonged plasma circulation and enhanced tumor accumulation, it is imperative to use polymeric carriers with increased Mw, which makes high-Mw biodegradable polymeric conjugates the most attractive candidates for future clinical applications (8, 9). Thus, we designed second-generation HPMA copolymer carriers that contain enzymatically degradable oligopeptide sequences in the linear main chain by combining reversible addition-fragmentation chain transfer (RAFT) polymerization and click reactions (10–12). In addition, we developed a new RAFT chain transfer agent (Peptide2CTA) composed of an enzymatically degradable oligopeptide sequence flanked by two dithiobenzoate groups. The monomer units incorporate in both positions at the same rate. Consequently, the process allows to synthesize well-defined degradable diblock copolymers with narrow polydispersity in one step (12), which is suitable for scale-up of the synthesis.

To date, ovarian cancer remains the deadliest gynecologic malignancy in the United States, with an estimated 15,500 deaths in 2012. The disease is usually diagnosed in advanced stages and the 5-y survival remains 44% for all stages and 27% for advanced stages (13). Because the majority of patients with this disease have advanced intraperitoneal metastatic disease at diagnosis, chemotherapy has been considered as an essential treatment. Previous clinical trials have already demonstrated that combinations of two or more drugs were more effective in the treatment of ovarian cancer than just one drug alone (14, 15). Paclitaxel (PTX) and gemcitabine (GEM) possess distinct mechanisms of anticancer effect; they are among the most common antineoplastic agents and potent combination regimens in clinics. Therefore, we hypothesized that the combination of second-generation degradable diblock HPMA copolymer-PTX and HPMA copolymer-GEM conjugates would present an efficient way to treat solid tumor.

Significance

In previous clinical testing, first-generation *N*-(2-hydroxypropyl)-methacrylamide (HPMA) copolymer-drug conjugates circumvented drug resistance and showed reduced side effects, although only minor improvement was seen in therapeutic efficacy. For effective clincial translation, second-generation high-molecular weight backbone-degradable HPMA copolymer carriers designed by our group sought to provide prolonged blood circulation and enhanced tumor accumulation to enable sufficient exposure of tumors to effective drug concentrations, and guarantee their biocompatibility by making polymer backbone degradable. The second-generation conjugates showed favorable pharmacokinetic profiles and controlled drug release, resulting in a dramatic improvement of therapeutic efficacy, as compared with first-generation conjugates and free drugs. For future industrial-scale manufacture, a new reversible addition-fragmentation chain transfer agent was developed that enables synthesis of conjugates in one step.

Author contributions: R.Z., J.Y., and J.K. designed research; R.Z., J.Y., M.S., and Y.Z. performed research; R.Z., J.Y., and J.K. analyzed data; and R.Z., J.Y., and J.K. wrote the paper.

Conflict of interest statement: J.Y. and J.K. have patent application pending related to technology cited in this work; J.K. has ownership in TheraTarget, Inc., which has licensed technology from the University of Utah related to polymer drug carriers.

This article is a PNAS Direct Submission.

[1]To whom correspondence should be addressed. Email: Jindrich.Kopecek@utah.edu.

This article contains supporting information online at www.pnas.org/lookup/suppl/doi:10.1073/pnas.1406233111/-/DCSupplemental.

To prove this hypothesis, we synthesized diblock backbone-degradable HPMA copolymer-PTX and HPMA copolymer-GEM conjugates (2P-PTX, 2P-GEM), respectively, and evaluated their combination as therapeutics against A2780 human ovarian carcinoma xenografts. Combination of first-generation low-Mw HPMA copolymer conjugates (P-PTX and P-GEM) and combination of free drugs (PTX and GEM) served as controls. In addition, studies of dual-labeled (^{125}I and ^{111}In; FITC and Cy5) model conjugates were performed to evaluate the fate of second-generation conjugates at whole-body, tissue, and cellular levels. The new generation degradable carriers with high Mw have a great potential to improve therapeutic performance and narrow the gap between preclinical studies and clinical trials (1, 2).

Results

Synthesis and Characterization of HPMA Copolymer-Drug Conjugates. The general approaches used for synthesis of HPMA copolymer-drug conjugates are depicted in Fig. 1 and detailed in *SI Materials and Methods*, Fig. S1, and Table S1. The use of the Peptide2CTA RAFT chain transfer agent (12) permitted one-step synthesis of diblock degradable HPMA copolymer-drug (PTX and GEM) conjugates with narrow Mw distribution. As shown in Fig. 1*B*, the diblock conjugates can be eliminated via renal filtration following enzymatic degradation. To monitor the fate of conjugates, we synthesized two sets of dual-labeled model conjugates: (*i*) dual-isotope–labeled conjugates and (*ii*) dual-fluorophore–labeled conjugates. For dual-isotope–labeled conjugates we incorporated into HPMA copolymer backbone a small amount of *N*-methacryloyltyrosinamide (MA-Tyr-NH_2) comonomer (16) and radioiodinated it with ^{125}I. To obtain information on in vivo drug delivery, we chose ^{111}In-DTPA complex to mimic drug (Fig. 1*C*). We attached a bifunctional chelating agent p-SCN-Bn-DTPA to cleavable tetrapeptide GFLG side chains via ethylenediamine linker and labeled it with ^{111}In (Fig. 1*C* and *SI Materials and Methods*). For dual-fluorophore–labeled conjugates, to label the backbone, we used a small amount of comonomer-containing FITC (termed as MA-FITC) (17). To mimic the drug, we incorporated the thiothiazolidine-2-thione (TT) containing comonomer (MA-GFLG-TT) and conjugated imaging probe Cy5 by polymer analogous reaction of TT groups with Cy5 amine (Fig. 1*D* and *SI Materials and Methods*).

In Vitro Cytotoxicity. The cytotoxicity of free drugs (PTX, GEM) and their HPMA copolymer conjugates (2P-PTX, 2P-GEM) against A2780 human ovarian cancer cells was determined. Representative cell-growth inhibition curves are shown in Fig. S2. Overall, free drugs (PTX, GEM) and their conjugates (2P-PTX, 2P-GEM) showed a dose-dependent cytotoxicity against A2780 cells. The IC_{50} values (Fig. 2*A*) revealed that HPMA copolymer-drug conjugates exhibited less cytotoxicity than their corresponding free drugs, which is because of different mechanisms of cell entry: diffusion (free drugs) vs. endocytosis (conjugates). If IC_{50} is calculated based on intracellular concentrations of drugs, the cytotoxicity of HPMA copolymer-drug conjugates may be equivalent to or higher than that of free drugs (18).

Cell Cycle Perturbation Following Different Exposure Schedules. In combination treatment, different administration sequences of drugs might lead to distinct interactions, ranging from antagonism to synergism (19–22). Because both PTX and GEM are cell cycle-specific drugs, we analyzed A2780 cell cycle changes after exposure to drug alone, conjugate alone, or different sequential combinations to investigate the schedule-dependence. Fig. 2*B* and Fig. S3 show the percentage of cells in the different phases of cell cycle. Histograms of DNA content (Fig. S3) revealed that PTX or 2P-PTX alone could induce accumulation of cells in the G2/M phase with a concomitant decrease in G0/G1 compartment, which was in agreement with the known response of other tumor cells to PTX (20–22). Similarly, GEM alone caused a reduction in the G0/G1 phase, with cells arresting mainly in S and G2/M phases (20–22). 2P-GEM did not dramatically alter cell cycle distribution like GEM, probably because of the relatively low dose (20 nM GEM equivalent) of conjugate applied within this experimental setting. Interestingly, PTX and its conjugate induced formation of hyperploidy (4N) (PTX: 14.2%, 2P-PTX: 7.3%), which involves abnormal chromatid segregation, incomplete cell division, and aberrant exit from mitosis to a G1-like stage of 4N cells (termed "mitotic slippery") (Fig. S3). Hyperploidy can be produced by prolonged exposure to microtubule inhibitor, like PTX. However, when GEM was given before or simultaneously with PTX, GEM arrested cells at G0/G1 phase and reduced PTX-induced hyperploidy (Fig. 2*B*) (21). Variant patterns of cell cycle distribution under different combination sequences revealed that the interaction between GEM and PTX is likely schedule-dependent.

Combination Effect of PTX and GEM. To determine synergistic, additive, or antagonistic interactions between PTX and GEM, we analyzed their combinations with different exposure sequences using the Chou–Talalay method (Table S2) (23). This procedure allows characterization of drug interactions with a single number, the Combination Index (CI). CI values of 0.9–1.1 indicate additivity, and CI values >1.1 or <0.9 were interpreted as antagonism

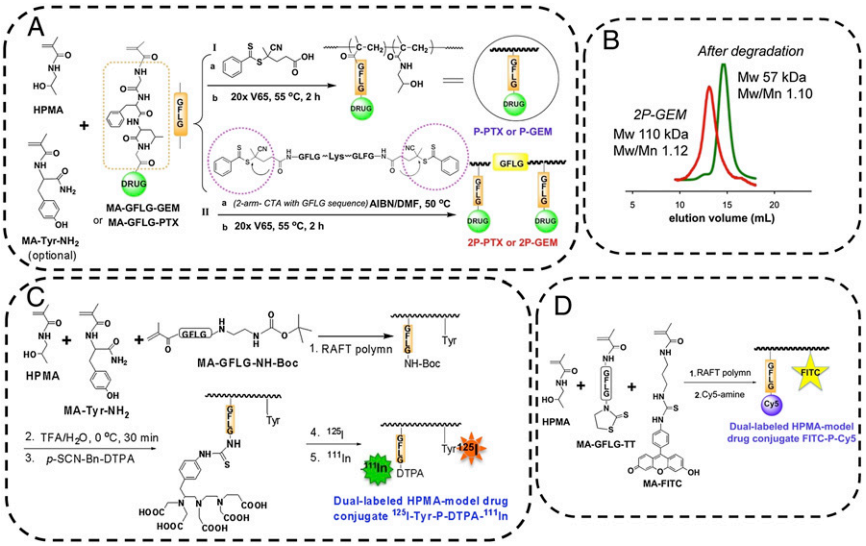

Fig. 1. Synthesis of HPMA copolymer-drug conjugates and dual-labeled model conjugates. (*A*) Synthesis of first-generation conjugate (P-GEM and P-PTX) using 4-cyanopentanoic acid dithiobenzoate as the RAFT chain transfer agent followed by end-modification with V65 (I), and synthesis of backbone degradable diblock conjugates (2P-GEM and 2P-PTX) using peptide2CTA as RAFT chain transfer agent (II). MA-Tyr-NH_2 was optionally used for ^{125}I labeling for pharmacokinetics and biodistribution studies. (*B*) Following incubation of 2P-GEM with papain, the Mw decreased to half of the original one. (*C*) Dual-isotope–labeled model conjugates were synthesized in multiple steps. Chelator DTPA was covalently attached to polymer backbone via GFLG cleavable linker to mimic the drug. The polymer precursor was then labeled with ^{125}I and ^{111}In. (*D*) Dual-fluorophore–labeled model conjugate was synthesized by RAFT copolymerization of HPMA with MA-GFLG-TT and MA-FITC followed by polymer analogous reaction with Cy5 amine.

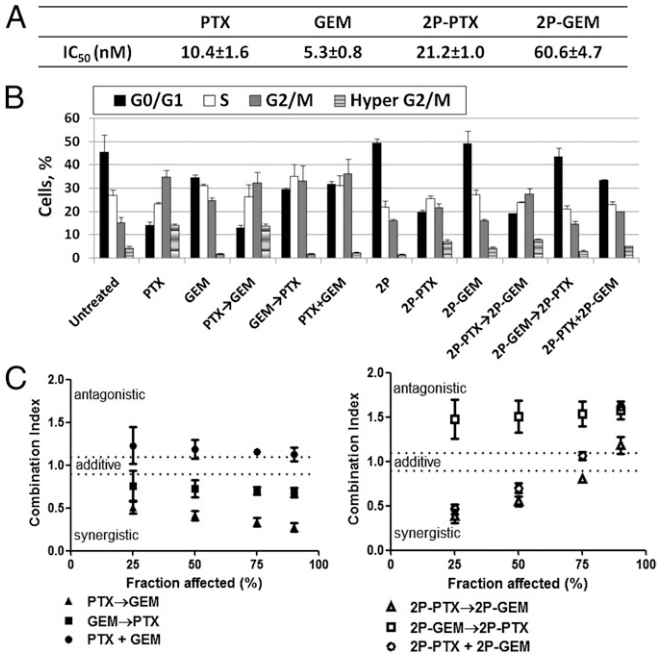

Fig. 2. Treatment with PTX followed by GEM showed strong synergism in vitro. (*A*) IC_{50} values of free drugs (PTX, GEM) and their conjugates (2P-PTX, 2P-GEM) toward A2780 cancer cells. (*B*) Percentage of A2780 cells in the different phases of cell cycle after single treatment or different sequential combinations. Cells were treated with 10 nM PTX or GEM in free-drug groups, or conjugates (20 nM equivalent PTX or GEM) in conjugate groups. (*C*) CI of PTX and GEM with different administration sequences. Cells were exposed to different sequential treatments, including free-drug combination and their conjugates combination. CI was calculated by the Chou–Talalay method. Data plotted are CI values at 25%, 50%, 75%, and 90% fraction killed. All of the data are expressed as mean ± SD ($n = 3$).

and synergism, respectively. The CI values of different sequential combinations are summarized in Table S3 and isobolograms were constructed for fraction affected (Fa, representing degree of growth inhibition) (Fig. 2*C*). In free-drug combinations, PTX followed by GEM (PTX→GEM) showed more potent cytotoxicity than the reverse sequence (GEM→PTX) or concurrent exposure (PTX+GEM) (Fig. 2*C*). Strong synergism was observed for the sequence PTX→GEM, with CI values ranging from 0.51 to 0.28 (Table S3). We also investigated these three schedules in conjugate combinations (i.e., 2P-PTX→2P-GEM, 2P-GEM→2P-PTX, and 2P-PTX+2P-GEM). The combinations showed synergistic effect (up to 70% Fa level) when 2P-PTX was given before or simultaneously with 2P-GEM, whereas posttreatment with 2P-PTX resulted in antagonism (Fig. 2*C*). Within the Fa levels from 75% to 90%, 2P-PTX→2P-GEM produced additive outcome, whereas antagonistic interaction occurred in the sequence 2P-PTX +2P-GEM. Both annexin V/7-AAD (7-aminoactinomycin D) apoptosis assay and cell migration/invasion assay supported the findings from CI experiments: (*i*) PTX→GEM (65.5%) induced more apoptosis than PTX+GEM (54.3%) (Fig. S4*A*) ($P < 0.05$), whereas there was no statistical difference between two synergistic sequences (PTX→GEM: 65.5% vs. GEM→PTX: 63.2%). In conjugate combination, both 2P-PTX→2P-GEM (65.6%) and 2P-PTX+2P-GEM (65.5%) showed significantly stronger cytotoxicity than antagonistic schedule 2P-GEM→2P-PTX (44.0%) ($P < 0.01$). (*ii*) Among all three administration sequences, PTX→GEM (30.9%) also displayed the strongest inhibition effect on A2780 cell migration (Fig. S4*B*) (GEM→PTX: 50.9%; PTX+GEM: 48.9%. $P < 0.01$). In addition, PTX→GEM (48.4%) was able to effectively inhibit cell invasion as well. Nevertheless, there was no statistically significant difference between PTX→GEM and the other two sequences (GEM→PTX; PTX+GEM). Overall, administration of PTX followed by GEM appears to be necessary for maximal augmentation of anti-tumor activity against A2780 cancer cells.

Pharmacokinetics and Imaging Studies of ^{125}I-labeled Conjugates. Before in vivo therapeutic evaluation, we compared pharmacokinetic profiles of first-generation low-Mw conjugates (P-PTX, P-GEM) and second-generation high-Mw diblock conjugates (2P-PTX, 2P-GEM). The blood radioactivity-time profiles of four conjugates in mice are illustrated in Fig. 3*A* and the pharmacokinetic parameters are summarized in Table S4. The previously reported half-lives of Cremophor EL-based PTX vehicle and GEM are cited here for comparison (24, 25). Both second-generation conjugates, 2P-PTX and 2P-GEM, showed improvement in pharmacokinetics. 2P-PTX showed a longer terminal half-life (37.90 h) than P-PTX (13.30 h), PTX (2 h), and Cremophor EL (17 h) (24). 2P-GEM (32.07 h) also had prolonged half-life compared with P-GEM (6.36 h) and GEM (1.2 h) (25). The total area under the blood concentration versus time curve (AUC) of 2P-PTX [1206% injected dose per milliliter (ID/mL)] was significantly higher than that of P-PTX (420% ID/mL) ($P < 0.001$). 2P-GEM (AUC = 1481% ID/mL) even had a 13-fold higher systemic exposure than P-GEM (108% ID/mL) ($P < 0.001$). The increased exposure resulted mainly from a significantly slower mean systemic clearance (CL) of second-generation conjugates (2P-PTX: 0.08 mL/h vs. P-PTX: 0.24 mL/h; 2P-GEM: 0.07 mL/h vs. P-GEM: 0.92 mL/h) ($P < 0.001$). In addition, the mean residence time of second-generation conjugates was also significantly longer than that of first-generation conjugates (2P-PTX: 52.86 h vs. P-PTX: 18.25 h; 2P-GEM: 45.39 h

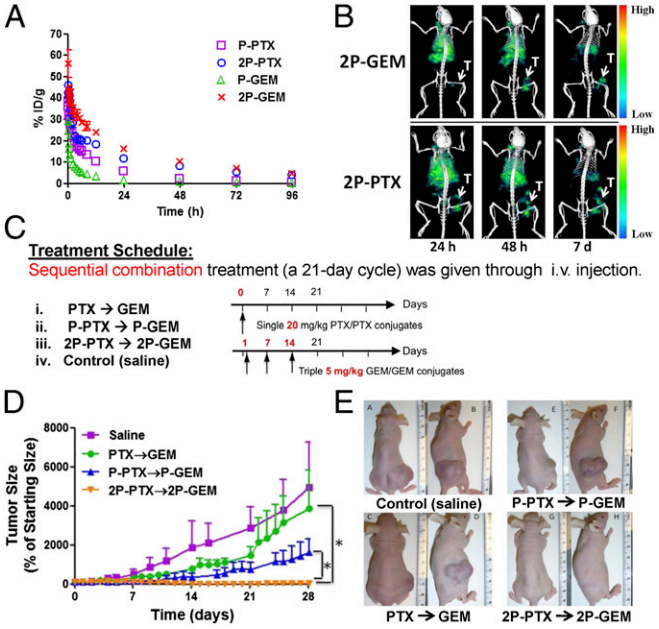

Fig. 3. Combination treatment of second-generation conjugates showed improved therapeutic efficacy in A2780 human ovarian carcinoma xenografts. (*A*) Blood activity-time profiles of ^{125}I-labeled conjugates in mice. The data represent the mean radioactivity expressed as a percentage of the injected dose per gram of blood from mice ($n = 5$). (*B*) SPECT/CT images of mice bearing subcutaneous A2780 tumor in right flank 24 h, 48 h, and 7 d after intravenous injection of ^{125}I-labeled conjugates (2P-PTX, 2P-GEM). T, tumor. (*C*) Experimental schedules of treatment in mice bearing A2780 tumor xenografts. Female nude mice received one dose of PTX or HPMA copolymer-PTX conjugate (20 mg/kg PTX equivalent) on day 0 and three doses of GEM or HPMA copolymer-GEM conjugate (5 mg/kg GEM equivalent) on days 1, 7, and 14. (*D*) A2780 tumor growth in mice treated with different formulation combinations ($n = 5$). *$P < 0.01$. Note: in the orange (2P-PTX→2P-GEM) line the error bars are hidden within the experimental points. (*E*) Photographs of A2780 tumors after treatment with different combinations.

vs. P-GEM: 8.49 h) ($P < 0.001$). Because of prolonged blood circulation time, the accumulation of ^{125}I-labeled conjugates (2P-PTX, 2P-GEM) at tumors was readily visualized in single-photon emission computed tomography (SPECT)/CT images 24 h after intravenous administration and further increased at 48 h because of the EPR effect (Fig. 3*B*) (7). At day 7, there was still a relatively high signal of ^{125}I-labeled conjugates remaining at the tumor compared with other tissues.

In Vivo Antitumor Activity. Therapeutic potential of second-generation conjugates was evaluated in female nude mice bearing A2780 human ovarian carcinoma xenografts. The combination index data shown above indicate that exposure of cells to PTX first followed by GEM results in a synergistic effect. Consequently, the mice were intravenously injected with one dose of PTX or HPMA copolymer-PTX conjugates (20 mg/kg PTX equivalent) on day 0, and three doses of GEM or HPMA copolymer-GEM conjugates (5 mg/kg GEM equivalent) on days 1, 7, and 14 (Fig. 3*C*). Tumor growth and ascites development were closely monitored during treatment (Fig. 3*D*). At day 21, complete tumor regression was achieved in two mice treated with the combination of second-generation conjugates (2P-PTX→2P-GEM), and relative tumor volume of the other three mice in this group decreased to 3% of initial size (Fig. 3*D*). Free-drug combination (PTX→GEM) and first-generation conjugate combination (P-PTX→P-GEM) at equivalent doses only produced a delay effect on tumor growth but no regressions, with 3,883 ± 1,937% and 1,612 ± 702% of baseline, respectively. At day 28, the differences of tumor size were statistically significant between 2P-PTX→2P-GEM and other combination group (Fig. 3 *D* and *E*) ($P < 0.01$). We also found that the mice treated with saline developed bloody ascites, whereas the mice treated with 2P-PTX and 2P-GEM had no detectable ascites. In addition, histological analysis showed that combination treatment of second-generation conjugates inhibited angiogenesis and proliferation of tumor cells and promoted more tumor cells to undergo apoptosis compared with saline treatment (Fig. S5). (*i*) Angiogenesis marker CD31, which indicates the presence of endothelial cells in blood vessels, showed that in mice treated with second-generation conjugates there was a smaller number of blood vessels and shorter length of blood vessels lumen. (*ii*) K_i-67 proliferation marker indicated that there was much less cell proliferation in tumors after 2P-PTX→2P-GEM treatment. (*iii*) TUNEL staining showed that more tumor cells underwent apoptosis in second-generation conjugate-treated tumor than in saline-treated tumor. For safety evaluation, body weight of the mice was also recorded during treatment (Fig. S6). The body weights recovered quickly after treatment withdrawal. By day 28, the mice treated with second-generation conjugates gained an average of 4.0% body weight, whereas the saline-treated mice gained 19.4%. The body-weight difference between saline-treated and conjugates-treated groups may be attributed to the difference of tumor weight and ascites. Fig. S5 shows that histopathologic features of major organs in mice treated with 2P-PTX→2P-GEM were similar to those observed in the saline-treated mice. No abnormal features were identified, indicating a favorable toxicity profile of combination treatment with second-generation conjugates.

Imaging Studies of Dual-Labeled Model Conjugates. To gain a deeper insight into fate of second-generation conjugates in the body and cancer cells, we used dual-labeled model conjugates, including ^{125}I-Tyr-P-DTPA-^{111}In and FITC-P-Cy5, and investigated their behavior at cell and animal levels. The dual-labeling strategy allowed us to separately track the payload (^{111}In-DTPA, Cy5) and polymeric carriers (^{125}I-Tyr-P, FITC-P) at the same time. The blood (radio)activity-time profile of model conjugate ^{125}I-Tyr-P-DTPA-^{111}In is illustrated in Fig. 4*A* and pharmacokinetic parameters are summarized in Table S5. We found that payload ^{111}In-DTPA and carrier ^{125}I-Tyr-P possess similar blood half-lives in mice (27.96 h vs. 30.68 h) (Table S5).

We also compared biodistribution of payload ^{111}In-DTPA and carrier ^{125}I-Tyr-P (Fig. 4*B*). At 48 h and 96 h after intravenous injection of conjugate ^{125}I-Tyr-P-DTPA-^{111}In, ^{111}In-DTPA showed similar uptake in major organs as ^{125}I-Tyr-P. It revealed that the GFLG bond between payload and backbone remained stable in the bloodstream during transport, which is in agreement with results obtained with isolated plasma (26). Dual-isotope SPECT/CT images in Fig. 4*D* showed that both ^{111}In-DTPA and ^{125}I-Tyr-P accumulated at the tumors. At 48 h after injection, the tumor uptake of ^{111}In-DTPA and ^{125}I-Tyr-P reached 4.08% injected dose per gram tissue (ID/g) and 4.57% ID/g (Fig. 4*C*), respectively. Notably, the tumor uptake of the second generation is significantly higher than that of first-generation low-Mw model conjugate (^{111}In: 0.77% ID/g, ^{125}I: 0.53% ID/g) (Fig. 4*C*) ($P < 0.001$). At the cellular level, we took 3D stochastic optical reconstruction microscopy (3D-STORM) images of model conjugate FITC-P-Cy5 to elucidate conjugate internalization and drug release. The high-resolution 3D-STORM imaging allowed us to track single molecules with ∼10-nm precision (below the diffraction limit) (27). As shown in Fig. 5, model conjugate FITC-P-Cy5 was internalized via endocytosis, and most FITC-P signal colocalized with lysosomes and late endosomes. At 4 h, the majority of FITC-P and Cy5 molecules were located at the outer space of the cytoplasm and FITC-P molecules were surrounded by clusters of Cy5 molecules. Over time, more Cy5 molecules were found inside the cell and located at a distance from FITC-P, indicating the release of Cy5 from polymer side chains. By 12 h, we found that Cy5 molecules diffused over the entirety of the cell. These images reveal that the GFLG bond can be cleaved in the lysosomes and subsequently the functional payload can translocate to the cytoplasm.

Discussion

As noted above, the second-generation conjugates completely surmounted the first generation in therapeutic efficacy (Fig. 3*D*). Such effective inhibition of tumor growth was attributed to several features: improved pharmacokinetic profile, enhanced bioavailablity of polymer-bound drugs, and synergistic action of PTX and GEM in combination. (*i*) For improved pharmacokinetic profile, increased Mw of the conjugates resulted in enhanced drug exposure to tumor cells (in Table S4, 2P-PTX: 2.9×AUC of

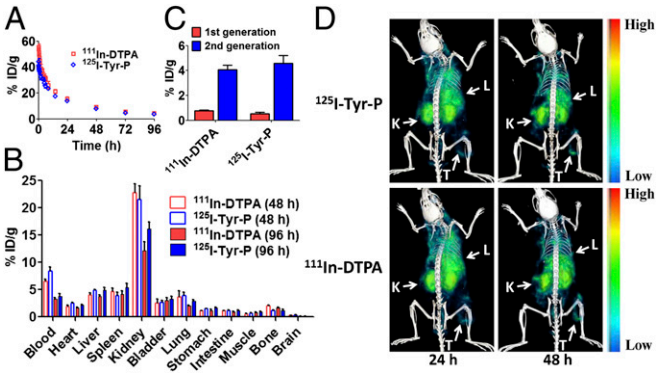

Fig. 4. ^{111}In-DTPA showed similar behavior as ^{125}I-Tyr-P in vivo after intravenous administration of second-generation conjugate ^{125}I-Tyr-P-DTPA-^{111}In. (*A*) Blood activity-time profiles of ^{111}In-DTPA and ^{125}I-Tyr-P in mice. The open circles represent the mean radioactivity expressed as a percentage of the injected dose per gram of blood from mice ($n = 5$). (*B*) Biodistribution of ^{111}In-DTPA and ^{125}I-Tyr-P in mice at 48 h and 96 h after injection of ^{125}I-Tyr-P-DTPA-^{111}In. (*C*) Tumor uptake of ^{111}In-DTPA and ^{125}I-Tyr-P in mice bearing subcutaneous A2780 tumor 48 h after injection of second-generation ^{125}I-Tyr-P-DTPA-^{111}In or first-generation model conjugates. Data obtained using the radioactivity count method plotted as percentage of injected dose per gram of tissue (% ID/g). All of the data are expressed as mean ± SD ($n = 4$–5). (*D*) Dual-isotope SPECT/CT images of ^{111}In-DTPA and ^{125}I-Tyr-P in mice bearing subcutaneous A2780 tumor in the right flank 24 h and 48 h after injection of ^{125}I-Tyr-P-DTPA-^{111}In. K, kidney; L, liver; T, tumor.

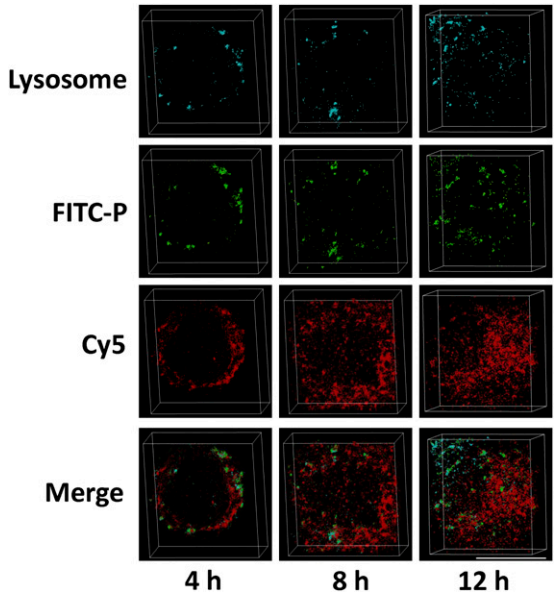

Fig. 5. High-resolution 3D-STORM images of endocytosis and drug release in A2780 cells after incubation with model conjugate FITC-P-Cy5 for 4 h, 8 h and 12 h. The lysosome in the cells was stained with LysoTracker Red DND-99. FITC, green; Cy5, red; LysoTracker, cyanine. (Scale bar, 10 μm.) Because of the high-localization precision and 3D image representation, a yellow color is not observed in the merged image.

P-PTX; 2P-GEM: 13.6×AUC of P-GEM). Notably, long retention time of drugs in the circulation is crucial to cell-cycle–specific drugs, which can exert effective actions on cells only during a specific phase of cell growth, such as PTX and GEM. (*ii*) Second, there is enhanced bioavailability of polymer-bound drugs. For example, GEM is rapidly metabolized to inactive 2-deoxy-2,2-difluorodeoxyuridine (dFdU) by cytidine deaminase present in the blood, liver, and other tissues (28). To maintain an adequate drug concentration in the patient's body, GEM is often administered at high doses through intravenous infusion. However, the use of anticancer drugs at high doses often exposes the patients to the risk of nonspecific acute toxicity, such as myelosuppression and reversible transaminase elevation with GEM, because of uncontrolled and random dissemination of the drugs in the body (29). Attaching GEM to HPMA copolymer dramatically decreases GEM's metabolism rate. (*iii*) Finally, there is synergistic action of PTX and GEM in combination. Because of the complexity of cancer, the synergistic combination of drugs, which have distinct and complementary mechanisms of action, is a feasible means to cure cancer. For example, PTX interacts with tubulin in cell cytoplasm, whereas GEM triphosphate replaces cytidine during DNA replication and causes replication arrest and apoptosis. Our CI study demonstrated that the combination of PTX and GEM is schedule-dependent and treatment with PTX followed by GEM has the strongest synergism (Fig. 2). One possible mechanism for the synergism of PTX→GEM is that the amount of microtubulin rapidly decreased in the tumor cells exposed to such sequential treatment. Generally in the tumor cells treated with PTX, an excess of microtubules is degraded and simultaneously a large amount of new tubulin is synthesized to support normal cell metabolism. If GEM is administered after PTX, GEM may incorporate into DNA, restrain transcription, and interrupt the synthesis of new tubulin. In addition, treatment with PTX can significantly increase the intratumoral concentration of GEM and the cellular content of the active triphosphate form of GEM, thus improving its efficacy (30, 31). Some clinical studies also demonstrated that combination treatment with PTX and GEM increased tumor regression rates compared with single-drug therapy, and sequential therapy with PTX followed by GEM was highly effective (32–34). Overall, all of the aforementioned features make this conjugate-mediated combination system superior to previously reported combination therapeutics against the same ovarian carcinoma (see *SI Discussion* for details).

This study used dual-labeled model conjugates to separately investigate behavior of carrier and payload. (*i*) To follow the in vivo fate of the conjugates, we tracked the dual-isotope–labeled model conjugate ^{125}I-Tyr-P-DTPA-^{111}In. HPMA copolymer backbone was labeled with ^{125}I, whereas ^{111}In-DTPA complex was bound at the oligopeptide GFLG side-chain termini and served as the drug model. The results demonstrated that payload (^{111}In) had similar blood half-life and tissue uptake as polymeric carrier (^{125}I), indicating the integrity of GFLG bond in blood circulation during transport (Fig. 4). The tumor accumulation of second-generation conjugate was five- (^{111}In) to eight- (^{125}I) times more efficient than accumulation of first-generation conjugates (Fig. 4*C*). (*ii*) To follow the conjugates at the cellular level, we used a fluorescently dual-labeled conjugate (FITC-P-Cy5). FITC served as the backbone tag and Cy5 was bound to the GFLG spacer as the model drug. Three-dimensional STORM images of FITC-P-Cy5 visualized endocytosis of intact conjugates and diffusion of drug model from lysosomes into the cytoplasm (Fig. 5), suggesting the specific cleavage of cathepsin B-sensitive GFLG linker and intracellular release of model drug. The GFLG segment between two HPMA copolymer blocks can be cleaved as well, leading to the degradation of polymer backbone. The expression of cathepsin B is tightly regulated in normal physiological conditions (35), and its expression increases in malignant ovarian and other tumors, which contributes to the degradation of extracellular matrix in the process of tumor cell invasion (36, 37). High expression of cathepsin B in tumor cells can lead to a fast release of drugs from conjugates (*SI Discussion*). As shown in Fig. 5, the drugs diffused over the entire cell at 12 h. Drug molecules that are released intracellularly may avoid the membrane efflux pumps, such as P-glycoprotein, and overcome efflux-pump–mediated drug resistance, as we previously observed (38). The results obtained with the dual-labeled model conjugates further demonstrated that second-generation conjugates possess favorable pharmacokinetics, preferential tumor accumulation, and controlled drug release, which are the most important factors to therapeutic index.

In summary, we designed and synthesized a new generation of backbone degradable diblock HPMA copolymer-PTX and HPMA copolymer-GEM conjugates. The in vitro studies demonstrated that the drug combination was sequence-dependent and PTX followed by GEM had synergism. The in vivo studies showed that second-generation backbone-degradable conjugates possessed prolonged blood-circulation time, enhanced tumor accumulation, and improved antitumor efficacy compared with first-generation low-Mw conjugates and free drugs. The new second-generation conjugates were degradable in vivo and possessed no obvious systemic toxicity. Thus, we anticipate that second-generation long-circulating degradable conjugates can open up new opportunities to improve current cancer chemotherapy.

Materials and Methods

A full description of materials and methods is provided in *SI Materials and Methods*.

IC_{50} Study and CI Analysis. In single treatment, A2780 cells were incubated with free drugs (PTX, GEM) or their conjugates (2P-PTX, 2P-GEM) at a series of drug concentrations for 24 h to assess IC_{50} of individual drug or conjugate. In combination treatment, A2780 cells were exposed to different sequential combinations (Table S2). The cell viability was measured by CCK-8 assay. Synergism, additivity, or antagonism of the combination was determined by the Chou–Talalay method.

Cell Cycle Analysis. A2780 cells were treated as shown in Table S2. After treatment, cells were fixed and stained with propidium iodide. Cell cycle analysis was performed using flow cytometer and FlowJo software.

High-Resolution 3D-STORM Imaging. A2780 cells were incubated with FITC-P-Cy5 for 4, 8, and 12 h at 37 °C, and stained with LysoTracker Red DND-99. Then, the cells were fixed with 4% (wt/vol) paraformaldehyde and visualized under a Vutara SR-200 fluorescence microscope.

Pharmacokinetics and Biodistribution Study. In pharmacokinetic study, female nude mice were intravenously injected with ^{125}I-Tyr-P-DTPA-^{111}In and ^{125}I-labeled conjugates, respectively. At predetermined time intervals, blood samples were taken from the tail vein and the radioactivity of each sample was measured with a Gamma Counter. As described previously (39), ^{125}I activity was counted in a channel with windows set for 15–85 keV and ^{111}In activity was counted in a channel of 237–257keV. The data were analyzed using a noncompartmental model with WinNonlin software. In a biodistribution study, female nude mice bearing A2780 ovarian carcinoma were intravenously injected with second-generation high-Mw conjugate ^{125}I-Tyr-P-DTPA-^{111}In and corresponding first-generation low-Mw model conjugate. At 48 h and 96 h after administration, various tissues were harvested, weighed, and counted for radioactivity with the aforementioned ^{111}In/^{125}I dual-isotope protocol. Uptake of the conjugate was calculated as the percentage of the injected dose per gram of tissue (% ID/g).

SPECT/CT Imaging. Dual-labeled ^{125}I-Tyr-P-DTPA-^{111}In and ^{125}I-labeled conjugates (2P-PTX, 2P-GEM) were intravenously injected into female nude mice bearing subcutaneous A2780 ovarian tumors. At 24 h and 48 h after administration, SPECT/CT images of mice were acquired by using an Inveon trimodality PET/SPECT/CT scanner. The data of ^{125}I image were histogrammed with a window setting of 15–85 keV, and the data of ^{111}In image used a window setting of 149–194 keV.

In Vivo Antitumor Activity. The mice in the drug-treated groups received sequential combination treatment as shown in Fig. 3*C* ($n = 5$), and the control mice received saline ($n = 5$). The tumor size was measured to monitor the tumor growth. The day that mice received PTX or its conjugates treatment was set as day 0 and the tumor volume at day 0 was normalized to 100%. All subsequent tumor volumes were expressed as the percentage relative to those at day 0. At the end of the experiment, the tumors were photographed and harvested for histological analysis.

Statistical Analysis. Data were presented as mean ± SD. Statistical analyses were done using a two-tailed unpaired Student *t* test, with *P* values of <0.01 indicating statistically significant differences.

ACKNOWLEDGMENTS. We thank Ruozhen Hu and Prof. Ryan O'Connell for assisting with flow cytometry analysis; Brian Watson and Prof. Edward W. Hsu for help with single-photon emission computed tomography/CT imaging study; Manasa Gudheti and Prof. Erik Jorgensen for Vutara Microscopy; Tian Yu for the assistance with PK analysis; and Sheryl Tripp in Associated Regional and University Pathologists, Inc. for histological staining. This work was supported in part by National Institutes of Health Grant CA156933 from the National Cancer Institute (to J.K.), and supported in conjunction with Grant P30 CA042014 awarded to the Huntsman Cancer Institute, University of Utah.

1. Kopeček J (2013) Polymer-drug conjugates: Origins, progress to date and future directions. *Adv Drug Deliv Rev* 65(1):49–59.
2. Kopeček J (2010) Biomaterials and drug delivery: Past, present, and future. *Mol Pharm* 7(4):922–925.
3. Kopeček J, Kopečková P (2010) HPMA copolymers: Origins, early developments, present, and future. *Adv Drug Deliv Rev* 62(2):122–149.
4. Vasey PA, et al.; Cancer Research Campaign Phase I/II Committee (1999) Phase I clinical and pharmacokinetic study of PK1 [*N*-(2-hydroxypropyl)methacrylamide copolymer doxorubicin]: First member of a new class of chemotherapeutic agents-drug-polymer conjugates. *Clin Cancer Res* 5(1):83–94.
5. Seymour LW, et al.; Cancer Research Campaign Phase I/II Clinical Trials committee (2002) Hepatic drug targeting: Phase I evaluation of polymer-bound doxorubicin. *J Clin Oncol* 20(6):1668–1676.
6. Seymour LW, et al. (2009) Phase II studies of polymer-doxorubicin (PK1, FCE28068) in the treatment of breast, lung and colorectal cancer. *Int J Oncol* 34(6):1629–1636.
7. Maeda H (2010) Tumor-selective delivery of macromolecular drugs via the EPR effect: Background and future prospects. *Bioconjug Chem* 21(5):797–802.
8. Seymour LW, Duncan R, Strohalm J, Kopeček J (1987) Effect of molecular weight (Mw) of *N*-(2-hydroxypropyl)methacrylamide copolymers on body distribution and rate of excretion after subcutaneous, intraperitoneal, and intravenous administration to rats. *J Biomed Mater Res* 21(11):1341–1358.
9. Shiah JG, et al. (2001) Biodistribution and antitumour efficacy of long-circulating *N*-(2-hydroxypropyl)methacrylamide copolymer-doxorubicin conjugates in nude mice. *Eur J Cancer* 37(1):131–139.
10. Yang J, Luo K, Pan H, Kopečková P, Kopeček J (2011) Synthesis of biodegradable multiblock copolymers by click coupling of RAFT-generated heterotelechelicPolyHPMA conjugates. *React Funct Polym* 71(3):294–302.
11. Luo K, Yang J, Kopečková P, Kopeček J (2011) Biodegradable multiblock poly[*N*-(2-hydroxypropyl)methacrylamide] via reversible addition-fragmentation chain transfer polymerization and click chemistry. *Macromolecules* 44(8):2481–2488.
12. Pan H, Yang J, Kopečková P, Kopeček J (2011) Backbone degradable multiblock *N*-(2-hydroxypropyl)methacrylamide copolymer conjugates via reversible addition-fragmentation chain transfer polymerization and thiol-ene coupling reaction. *Biomacromolecules* 12(1):247–252.
13. American Cancer Society (2012) *Cancer Facts and Figures 2012* (American Cancer Society, Atlanta).
14. Mutch DG (2003) Gemcitabine combination chemotherapy of ovarian cancer. *Gynecol Oncol* 90(2 Pt 2):S16–S20.
15. Ozols RF (2000) Paclitaxel (Taxol)/carboplatin combination chemotherapy in the treatment of advanced ovarian cancer. *Semin Oncol* 27(3, Suppl 7):3–7.
16. Lee JH, Kopečková P, Kopeček J, Andrade JD (1990) Surface properties of copolymers of alkyl methacrylates with methoxy (polyethylene oxide) methacrylates and their application as protein-resistant coatings. *Biomaterials* 11(7):455–464.
17. Omelyanenko V, Kopečková P, Gentry C, Kopeček J (1998) Targetable HPMA copolymer-adriamycin conjugates. Recognition, internalization, and subcellular fate. *J Control Release* 53(1-3):25–37.
18. Minko T, Kopečková P, Kopeček J (1999) Comparison of the anticancer effect of free and HPMA copolymer-bound adriamycin in human ovarian carcinoma cells. *Pharm Res* 16(7):986–996.
19. Oliveras-Ferraros C, et al. (2008) Sequence-dependent synergism and antagonism between paclitaxel and gemcitabine in breast cancer cells: The importance of scheduling. *Int J Oncol* 32(1):113–120.
20. Kroep JR, et al. (2000) Sequence dependent effect of paclitaxel on gemcitabine metabolism in relation to cell cycle and cytotoxicity in non-small-cell lung cancer cell lines. *Br J Cancer* 83(8):1069–1076.
21. Sui M, Xiong X, Kraft AS, Fan W (2006) Combination of gemcitabine antagonizes antitumor activity of paclitaxel through prevention of mitotic arrest and apoptosis. *Cancer Biol Ther* 5(8):1015–1021.
22. Zupi G, et al. (2005) Potentiation of the antitumoral activity of gemcitabine and paclitaxel in combination on human breast cancer cells. *Cancer Biol Ther* 4(8):866–871.
23. Chou TC, Talalay P (1984) Quantitative analysis of dose-effect relationships: The combined effects of multiple drugs or enzyme inhibitors. *Adv Enzyme Regul* 22:27–55.
24. Sparreboom A, van Tellingen O, Nooijen WJ, Beijnen JH (1996) Nonlinear pharmacokinetics of paclitaxel in mice results from the pharmaceutical vehicle Cremophor EL. *Cancer Res* 56(9):2112–2115.
25. Beumer JH, et al. (2008) Plasma pharmacokinetics and oral bioavailability of 3,4,5,6-tetrahydrouridine, a cytidine deaminase inhibitor, in mice. *Cancer Chemother Pharmacol* 62(3):457–464.
26. Rejmanová P, Kopeček J, Duncan R, Lloyd JB (1985) Stability in rat plasma and serum of lysosomally degradable oligopeptide sequences in *N*-(2-hydroxypropyl) methacrylamide copolymers. *Biomaterials* 6(1):45–48.
27. Huang B, Wang W, Bates M, Zhuang X (2008) Three-dimensional super-resolution imaging by stochastic optical reconstruction microscopy. *Science* 319(5864):810–813.
28. Immordino ML, et al. (2004) Preparation, characterization, cytotoxicity and pharmacokinetics of liposomes containing lipophilic gemcitabine prodrugs. *J Control Release* 100(3):331–346.
29. Fossella FV, et al. (1997) Maximum-tolerated dose defined for single-agent gemcitabine: A phase I dose-escalation study in chemotherapy-naive patients with advanced non-small-cell lung cancer. *J Clin Oncol* 15(1):310–316.
30. Von Hoff DD, et al. (2011) Gemcitabine plus nab-paclitaxel is an active regimen in patients with advanced pancreatic cancer: A phase I/II trial. *J Clin Oncol* 29(34):4548–4554.
31. Kroep JR, et al. (1999) Gemcitabine and paclitaxel: Pharmacokinetic and pharmacodynamic interactions in patients with non-small-cell lung cancer. *J Clin Oncol* 17(7):2190–2197.
32. Saif MW (2013) U.S. Food and Drug Administration approves paclitaxel protein-bound particles (Abraxane®) in combination with gemcitabine as first-line treatment of patients with metastatic pancreatic cancer. *JOP* 14(6):686–688.
33. De Pas T, et al. (2006) A proper schedule of weekly paclitaxel and gemcitabine combination is highly active and very well tolerated in NSCLC patients. *Lung Cancer* 54(3):359–364.
34. Roy V, LaPlant BR, Gross GG, Bane CL, Palmieri FM; North Central Cancer Treatment Group (2009) Phase II trial of weekly nab (nanoparticle albumin-bound)-paclitaxel (nab-paclitaxel) (Abraxane) in combination with gemcitabine in patients with metastatic breast cancer (N0531). *Ann Oncol* 20(3):449–453.
35. Yan S, Sloane BF (2003) Molecular regulation of human cathepsin B: Implication in pathologies. *Biol Chem* 384(6):845–854.
36. Szpaderska AM, Frankfater A (2001) An intracellular form of cathepsin B contributes to invasiveness in cancer. *Cancer Res* 61(8):3493–3500.
37. Nishikawa H, et al. (2004) The role of cathepsin B and cystatin C in the mechanisms of invasion by ovarian cancer. *Gynecol Oncol* 92(3):881–886.
38. Minko T, Kopečková P, Pozharov V, Kopeček J (1998) HPMA copolymer bound adriamycin overcomes MDR1 gene encoded resistance in a human ovarian carcinoma cell line. *J Control Release* 54(2):223–233.
39. Carney PL, Rogers PE, Johnson DK (1989) Dual isotope study of iodine-125 and indium-111-labeled antibody in athymic mice. *J Nucl Med* 30(3):374–384.